The role of void space geometry in permeability evolution in crustal rocks at elevated pressure.

Philip M Benson[1,2], Philip G Meredith[1] and Alexandre Schubnel[2,*]

Contact: p.benson@ucl.ac.uk

[1] Mineral, Ice and Rock Physics laboratory, Department of Earth Sciences, University College London, Gower Street, London, WC1E 6BT, U.K.

[2] Lassonde Institute (Room 108), University of Toronto, 170 College Street, Toronto, Ontario, M5S 3E3, CANADA.

[*] Now at: Laboratoire de Geologie, Ecole Normale Superieure de Paris, 24 Rue Lhomond, 075005, Paris, FRANCE.

Abstract

A key consequence of the presence of void space within rock is their significant influence upon fluid transport properties. In this study, we measure changes in elastic wave velocities (P and S) contemporaneously with changes in permeability and porosity at elevated pressure for three rock types with widely different void space geometries: a high-porosity sandstone (Bentheim), a tight sandstone (Crab Orchard), and a microcracked granodiorite (Takidani). Laboratory data is then used with the permeability models of Guéguen and Dienes and Kozeny-Carman to investigate the characteristics that different void space geometries impart to measured permeabilities. Using the Kachanov effective medium theory, elastic-wave velocities are inverted, permitting the recovery of crack density evolution with increasing effective pressure. The crack densities are then used as input to the microcrack-permeability model of Guéguen and Dienes. The classic Kozeny-Carman approach of Walsh and Brace is also applied to the measured permeability data via a least squares fit in order to extract tortuosity data. We successfully predict the evolution of permeability with increasing effective pressure, as directly measured in experiments, and report the contrast between permeability changes observed in rock where microcracks or equant pores dominate the microstructure. Additionally, we show how these properties are affected by anisotropy of the rock types via the measured anisotropic fabrics in each rock. The combined experimental and modeling results illustrate the importance of understanding the details of how rock microstructure changes in response to an external stimulus in predicting the simultaneous evolution of different rock physical properties.

1. Introduction

Data from deep seismic soundings, borehole logging and laboratory measurements all indicate that porosity is a ubiquitous feature of most crustal rocks. This observation is fundamental to our understanding of crustal evolution and energy resource management, for example the efficient recovery of hydrocarbon and water resources, and the safe disposal of hazardous waste. This is because the transport and mechanical properties of crustal rocks are heavily influenced by porosity and its geometry; for example, the proportion of high aspect ratio pores to low aspect ratio cracks, and their connectivity. However, the processes responsible for porosity formation are diverse, ranging from depositional processes such as sorting and grain alignment, through diagenetic processes such as compaction and cementation, to deformational processes such as microcracking (e.g. Brace, 1980; Bourbie and Zinszner, 1985; Benson et al., 2003; Benson et al., 2005). The porosity that evolves from the superposition of these processes over time may therefore have a complex geometry or fabric. In addition, many of these processes have an inherent directionality which may lead to anisotropy of the void space, and all have been shown to play important roles in influencing the fluid transport properties of rock (Lo et al., 1986; Jones and Meredith, 1998; Rasolofosaon and Zinszner, 2002).

The measurement of permeability at elevated pressure and the calculation of permeability from other data (such as elastic wave velocities) remains non-trivial. In particular, in order to test models that attempt to predict such relations, both elastic wave velocities and permeability should ideally be measured simultaneously. We have done this in the study reported here. We then employ the simple Kozeny-Carman permeability model (Carman, 1961; Scheidegger, 1974; Guéguen and Palciauskas, 1994). This model was one of the first which attempted theoretically to derive an expression linking bulk porosity to permeability; via simplified key parameters of porosity, internal surface area, and an idealised pore/crack geometry representing either by an array of cylindrical capillaries or an array of

penny-shaped cracks (Brace et al., 1968). Additionally, we include the critical porosity modification of Mavko and Nur (1997) which introduces a porosity below which no fluid flow is possible. We then apply the modified model to our experimentally measured porosity and permeability data, and extract information on tortuosity for comparison to measured principal anisotropy axes and the observed pore fabric.

Elastic wave velocity measurement is a commonly used tool for studying both low and high aspect ratio void space in rock. However, low aspect ratio voids (e.g. microcracks) are known to exert a disproportionate influence on wave velocities (Bourbie and Zinszner 1985; Klimentos, 1991; Benson et al., 2003), and their anisotropy. We have used P and S-wave velocities to evaluate the decrease in crack density with increasing effective pressure. The Kachanov (1994) effective medium model has been employed to calculate crack densities (Guéguen and Schubnel, 2003; Benson et al., 2005). The calculated crack densities can be directly related to pore space connectivity, and thus to fluid permeability, using the statistical approach of Guéguen and Dienes (1989) which assumes a network of penny-shaped cracks embedded in an impermeable matrix. Using statistical physics together with a connectivity probability factor (percolation factor), the model calculates the equivalent effective area (and hence permeability) based upon the fluid movement through the network of linked cracks. The theoretically determined permeabilities are then directly compared to the actual steady-state flow permeabilities measured simultaneously with the elastic wave velocities. This combined approach is applied to three rocks with contrasting void space geometries in order to explore the differing roles that microcracks, equant pores and a mixture of the two exert on fluid permeability.

2. Sample Characteristics

In order to study the key influence of microstructural variation, we have chosen three rock types with strongly contrasting void space geometries. (1) Bentheim sandstone (BHS) from the Lower Saxony Basin, north-west Germany, is an off-white sandstone with a porosity of 23.0% (Klein et al., 2001; Benson, 2004). Mineralogically, it is a fairly pure quartzite (>97% quartz), with dominantly sub-rounded quartz grains approximately 0.25mm in diameter, cemented by siliceous cement. Only minor amounts of accessory minerals are present, including variably altered orthoclase feldspars, sparse grains of plagioclase (exhibiting multiple twinning) and microcline. The void space is comprised of predominantly near-equant pores. (2) Crab Orchard sandstone (COS) from the Cumberland Plateau, Tennessee (USA), is a red, fine-grained, cross-bedded fluvial sandstone. Grains are generally subhedral to sub-rounded, exhibit no preferred alignment (Benson et al., 2003), and have a mean size of approximately 0.25 mm. Porosity is 4.7%. Compositionally the rock is 85% quartz with numerous accessory minerals, including; 10 to 12% orthoclase feldspar (variably altered to sericite), 1 -2% lithic clasts and polycrystalline quartz, 5% clay minerals (predominantly iron rich clays with some sericite and a small amount of chlorite), and 1 to 2% muscovite with some phengite mica. Cementation is thought to have occurred early on in diagenesis, as nearly all grains show triple junctions, with few point contacts. The rock is compositionally and texturally mature, with a reasonable degree of compaction. There is definite alignment of mica flakes parallel to the bedding, and some micas also show kinking along the same direction, i.e. they have aligned preferentially with their long axes parallel to the bedding and have then been deformed along that direction, as a likely result of compaction, flow or flocculation (Stearns, 1954). A cement comprising sericitic clay, calcite, iron oxide and mica is abundant. The cement appears to have destroyed much of the original porosity, which is now characterized by a mixture of cracks and pores. (3) Takidani ‘granite’ (TDG) is a coarse grained granodiorite from the Japan Alps. Mineralogically, the rock is 30% quartz, 55% feldspar and ~10% amphibole, with between 5 and 8% biotite. Quartz grains are anhedral, roughly equi-granular, and generally in the size the range 0.5mm to 1mm. Some crystals contain fluid inclusions, and there is also

some evidence of magma mixing. TDG was formed at depth, where the relatively slow cooling rate under tectonic stress resulted in a void space that predominantly comprises aligned microcracks. This, in turn, has led to anisotropy in the physical and transport properties (Benson, 2004).

The 3-D geometry of all three pore fabrics were verified through measurements of the anisotropy of magnetic susceptibility of samples saturated with magnetic ferrofluid (pAMS; Benson et al., 2003). In the case of TDG, which contains a high natural matrix susceptibility, the dry matrix AMS measurements were subtracted from the ferrofluid-saturated rock measurements in order to obtain the void space AMS (pAMS). This method produces results that are entirely consistent with ultrasonic Vp and Vs measurements (Benson, 2004). The pAMS technique enabled the principal anisotropy axes to be determined for each rock, and these are shown in Figure 1. The minimum principal anisotropy directions were aligned normal or sub-normal to large scale bedding, cross-bedding, and the dominant microcrack plane for BHS, COS and TDG respectively (Benson et al., 2003; Benson, 2004; Benson et al., 2005).

3. Experimental Equipment and Methods

In order to eliminate potential errors caused by sample variability, we would ideally like to measure all the parameters of interest at the same time on the same sample under the same conditions. We therefore use an apparatus with the capability of measuring contemporaneous changes in elastic wave velocities (P and S), porosity, and permeability at elevated pressure (Jones & Meredith, 1998; Benson 2004; Benson et al., 2005). The apparatus comprises a 300 MPa hydrostatic pressure vessel equipped with dual 70 MPa servo-controlled pore fluid intensifiers. The intensifiers provide high pressure pore fluid (distilled water in this study) to each end of the test sample, and are fitted with

integral displacement transducers which enable them also to act as pore volumometers. Permeability measurements were made using the steady-state flow technique. A small, constant, pressure difference is imposed across the sample and, once steady-state flow is established, permeability can be calculated simply from the flow rate and the sample dimensions via direct application of Darcy's law. For all the experiments reported here, the pressure difference across the sample was 0.5 MPa and the mean pore fluid pressure was 2.5 MPa. All samples comprise cores that are 38.1mm in diameter and 40mm in length. Since all of the rocks used are known to be more or less anisotropic from pAMS measurements (Benson et al., 2003; Benson, 2004), cores samples were taken along the three known principal anisotropy directions (Figure 1).

4. Modeling Permeability

Permeability is one of the most important properties of porous rock, but is also one of the most difficult to examine theoretically. Although a trend is frequently observed between bulk porosity and permeability of sandstones (e.g. Brace, 1968; Bourbie and Zinszner, 1985; Guéguen and Palciauskas, 1994), there exists, in general, no simple relationship between permeability and commonly measured petrophysical parameters of porous media, such as porosity and elastic wave velocity (Guéguen and Palciauskas, 1994). Where such relationships have been established, they are often specific to the particular rock under investigation, and apply only over a limited range of conditions (e.g. Dullien, 1979; Bourbie and Zinzner, 1985; Klimentos, 1991; Bernabe et al., 2003). In addition, the range of pore fabric geometries over which such models can produce reasonable predictions is poorly known, due to the many ways in which pore fabric geometry, and hence connectivity, can be arranged. Two widely used permeability models are examined in this study, in order to explore the role which known, but different, pore fabrics play in permeability evolution at elevated pressure.

4.1 Kozeny-Carman Relation

One of the oldest and simplest attempts at deriving an expression linking bulk porosity to permeability is based upon hydraulic radius approximations, and gives rise to the Kozeny-Carman relation (e.g. Carman, 1961; Scheidegger, 1974; Guéguen and Palciauskas, 1994). An estimate of the permeability is made using simplified key parameters of porosity, internal pore space surface area, and an idealized pore fabric geometry represented by an array of intersecting cylindrical capillaries:

$$k \propto \frac{\phi^3}{S^2}$$

where, k is permeability and ϕ is porosity. S is the ratio of internal pore space surface area to rock volume, given by: $S = \frac{S_{pore}}{V_{solid}} = \frac{3}{2}\frac{(1-\phi)}{d}$, where d is a characteristic pore dimension (pore diameter in this case), S_{pore} is the internal pore surface area and V_{solid} is the volume of the solid sample, calculated using a simple packing of spherical grains (e.g. Mavko et al., 1998).

Substituting for S gives:

$$k \propto \frac{\phi^3}{(1-\phi)^2} d^2$$

However, no flow is possible below some critical porosity, also known as the percolation threshold, which is denoted ϕ_c (Mavko and Nur, 1997). This notion is also consistent with many crack models (e.g. Brace et al., 1968; Brace, 1980). Mavko and Nur (1997) show that this assumption modifies the basic Kozeny-Carman relation, above, to:

$$k \propto \frac{(\phi-\phi_c)^3}{\left[1-(\phi-\phi_c)\right]^2} d^2$$

Finally, the constant of proportionality which relates permeability to porosity is evaluated using the simple derivation of Walsh and Brace (1984), which then gives:

$$k = \frac{c}{b}\frac{(\phi - \phi_c)^3}{\tau^2}\frac{d^2}{\left[1-(\phi-\phi_c)\right]^2} \qquad (1)$$

Where c is a constant which depends upon the pore geometry (for spherical grains, c=9/4), and b is a crack parameter which varies between 2 for capillaries to 3 for penny-shaped cracks (Walsh and Brace, 1984). Therefore, in this work, we use b = 2 for BHS, and b = 3 for TDG. For COS, where the voids comprise a mixture of capillaries and cracks, we use b = 2.5. The tortuosity parameter τ is commonly visualized as the ratio of the total fluid flow path L length to the length of the sample L_0. This is strictly incorrect, since τ is not a geometrical factor, but is mathematically related to the pore phase percolation factor, $f_{pores} \approx 1/\tau^2$. Despite this technical limitation, in this work the former representation is used since it provides a useful qualitative indication of the changing geometry of the void space with increasing pressure.

Equation (1) can now be applied directly to experimental data (described below) under elevated effective pressures, using the measured rock porosity and permeability, with average pore diameter determined from mercury porosimetry (Figure 2A) and image analysis. Equation (1) is then inverted by means of experimental porosity-permeability data using a least square method in order to recover both the percolation threshold (ϕ_c) and the tortuosity (τ).

However, as noted previously, the experimental study presented here uses effective pressure as a primary control, rather than porosity. As the Kozeny-Carman model uses porosity as the primary

input for permeability calculation (Equation 1), then a method for relating the experimentally measured porosity data with the effective pressure must be established. This relation is available in the form of the measured porosity-pressure data for each rock (Figure 2B), which are fit with either polynomial or exponential regressions. These mathematical relationships are then used for calculation of effective pressure from the Kozeny-Carman calculated porosity/permeability model, thus allowing easy comparison of Kozeny-Carman predicted data to the measured laboratory data.

4.2 Pore and Crack Models

Simple capillary and pore based permeability models, as typically applied to highly porous rocks, have been around for many years (e.g. Guéguen and Palciauskas, 1994). By considering a connected network of capillaries, as formed by a close packing of rock grains, the following expression can be derived linking pore permeability (k_{pores}) to porosity (Guéguen and Palciauskas, 1994):

$$k_{pores} = \frac{1}{32} f_{pores} \bar{r}^2 \phi \qquad (2)$$

where, f_{pores} is the percolation factor, $\bar{r}$ is the average capillary radius and ϕ is the porosity. Theoretically, the percolation factor is intrinsically linked to the tortuosity by $f_{pores} \approx 1/\tau^2$ (Guéguen and Palciauskas 1994). In the following discussion, however, we assume that $f_{pores} \approx 1$ for BHS, due to its open and interconnected equant pore structure (Benson et al., 2005).

In contrast, the Guéguen and Dienes (1989) crack permeability model primarily takes into account low aspect ratio void space, or cracks, and proceeds in the following manner. Any crack represents a void space of non-zero size, with the aperture being defined as the maximum width. If the cracks intersect, this will produce a crack permeability based on the fluid movement through the

network of linked crack elements. Guéguen and Dienes (1989) quantify the effect of penny shaped cracks on the permeability of an otherwise impermeable host matrix, and derive the following relation:

$$k_{cracks} = \frac{2}{15} f_{cracks} w^2 \zeta \rho \qquad (3)$$

Where, ρ is the crack density, w and ζ are the crack aperture and average aspect ratio (ratio of crack aperture to crack length), respectively, and f_{cracks} is the percolation factor (Guéguen and Dienes, 1989), approximated via: $f_{cracks} \approx \frac{9}{4}\left(\frac{\pi^2}{4}\rho - \frac{1}{3}\right)^2$, and valid for $1/3 < \rho\pi^2/4 < 1$. In essence, f_{cracks} describes the probability of two cracks intersecting ($\rho\pi^2/4$), in which case the volume element created by the intersecting cracks is discounted in the method (an excluded volume). In all cases, $0 \leq f_{cracks} \leq 1$.

In the most simple case, the crack and near-equant porosity evolutions with pressure are decoupled. Indeed, the first is very compliant while the second is not. The simplest assumption for a rock containing both pores and cracks is therefore to assume that the total permeability (k) is the volume averaged sum of the crack and pore permeabilities:

$$k = k_{pores} + k_{cracks} \qquad (4)$$

Obviously, such a concept is an oversimplification since it neglects connectivity issues between the two kinds of porosity. It is obviously possible to arrange the connectivity in porous rock in an almost infinite number of ways, and in a 3-D rock volume it is likely such connectivity is manifested as an array of pore/crack elements arranged in series with strings of such elements connected in parallel (or vice-versa). However, to avoid getting into a potentially long and protracted argument discussing the

complexities of pore connectivity (which is beyond the scope of the present work), we thus concentrate on the simplified model above. As we shall see later, even a simple model can provide useful insight in helping estimate which factors dominate the bulk permeability and the permeability changes.

5. Experimental Results

5.1 Elastic Wave Velocity Measurements to Infer Crack Parameters

The evolution of crack permeability with increasing effective pressure is evaluated using an effective pressure – crack density (ρ) relationship for each rock type. As shown by equation (3), the crack-related permeability depends on the crack density and the crack aspect ratio, as first order parameters. These in turn can be determined from the inversion of elastic wave velocity measurements using a least square method via effective medium theories of solids containing penny shaped cracks. We used experimentally measured P-wave and S-wave velocity data (Figures 3, 4 and 5 and Tables 1, 3, 5 for BHS, COS and TDG respectively) and equation (3) to invert the data for crack density evolution with pressure. We use the Kachanov (1994) model (Kachanov, 1980; Sayers and Kachanov, 1995; Schubnel and Guéguen, 2003, Schubnel et al., 2005, Benson et al. 2006) which assumes that water-saturated, non-interacting microcracks, with a transversely isotropic alignment, are responsible for producing the measured elastic anisotropy change with effective pressure (see Kachanov 1994; Sayers and Kachanov, 1995; Schubnel and Guéguen, 2003, Schubnel et al., 2005).

To ensure stability in the Kachanov inversion, appropriate initial values of aspect ratio 'ζ_i' were assigned to each rock type, as follows: 0.0012 for BHS; 0.00068 and 0.00058 for COS, parallel and normal to the transverse isotropy (TI) plane respectively; and 0.00047 and 0.00042 for TDG, parallel

and normal to the TI plane respectively. For this estimation, the method of Morlier (1971) was employed, as described by Zimmerman (1991). Briefly, the laboratory Vp and Vs data are used to calculate the compressibility of the rock at each pressure step. These data are fit to an exponential decay, the exponent of which can be used to determine an aspect ratio distribution function $c(\alpha)$ as a function of aspect ratio, taking the form $c(\alpha) = C\alpha \exp(-\alpha / A)$, where α is aspect ratio, and A and C are constants calculated from the Morlier (1971) method (Zimmerman, 1991). The same values of rock (matrix) Young's modulus E_0 and Poisson's ratio υ_0 are used for this calculation and for the Kachanov crack density inversion (Tables 2, 4, 6). With knowledge of both the aspect ratio and the crack density, equation (3) may then be evaluated at each effective pressure for a given crack aperture.

5.2 Permeability Measurements

Figure 6A shows permeability data for Bentheim sandstone as a function of effective pressure in three orthogonal directions (labeled X, Y, and Z). Permeability does not change significantly with either flow direction or effective pressure. These experimental observations are consistent with the BHS microstructure and our pAMS data reported earlier. When modelling the permeability of BHS, the Kozeny-Carman approach fits the data reasonably well with a critical porosity of 0% and a tortuosity in the range 4.1 to 4.5. This appears entirely reasonable, given that the simple case of a cubic lattice of cylindrical pores yields a tortuosity of 3. Using the contemporaneous elastic wave velocity data, which is highly sensitive to microcracks, crack density decrease with increasing effective pressure is computed via the Kachanov model, as described above (Schubnel and Guéguen, 2003; Benson, 2004; Benson et al., 2006). The decrease in crack density with pressure can be interpreted as a decrease in the average apparent crack radius, due to an increase of contacts on the crack surfaces (Schubnel et al.,

2005). Due to the make-up of BHS, it is likely that this represents intergranular microcracking. By empirically assigning a family of crack apertures to this data, the effect of microcracks on permeability evolution is calculated for comparison with the experimentally measured data using the Guéguen and Dienes model (Figure 6B). In order to compare the small permeability changes due to crack closure to the measured data, a constant offset of k_{pores} = 0.81x10^{-12} m^2 needs to be added to the crack permeability. Assuming $f_{pores} \approx 1$ (approximating a fully connected pore space), equation (2) may then be used to estimate an average capillary diameter of ≈23 μm. This approach suggests that the crack permeability does not contribute significantly to the overall bulk permeability, but does contribute significantly to its small variation with pressure. As expected, the near-equant porosity dominates the overall permeability, while crack closure dominates the permeability change. This result agrees well with the crack aperture range of between 5 and 30 μm derived from the Kachanov/Guéguen and Dienes microcrack permeability approach, and fits the experimentally measured permeability data over the entire effective pressure range. This is further supported by mercury porosimetry data, which yields an average pore diameter of approximately 32 μm (Figure 2A).

Unlike BHS, Crab Orchard sandstone displays a high level of permeability anisotropy, with permeability measured sub-parallel to the cross-bedding (XY plane) more than twice that measured sub-normal to cross-bedding (Z axis), as shown in Figure 7A. In addition, the permeability decreases by more than an order of magnitude over the effective pressure range studied. In general, the Kozeny-Carman model provides a good fit to the experimental data. Using a least squares fit, a tortuosity of 0.012 (X) and 0.014 (Y) is calculated for fluid flow sub-parallel to the cross-bedding, whilst for permeability sub-normal to the cross-bedding (Z) the tortuosity is 0.028. These results are as intuitively expected, with a lower tortuosity corresponding to higher permeability along the cross-bedding layers, and vice versa. The average critical porosity is calculated as ϕ_c = 4.2%.

Figure 7B shows the results of the Guéguen and Dienes model fits for COS. In order to fit the permeability anisotropy, two separate populations of crack apertures are needed; from 0.8 μm - 1.2 μm sub-normal to the cross-bedding (ζ_i = 0.00058) , and 1.3 μm - 1.9 μm sub-parallel to the cross-bedding (ζ_i = 0.00068). As for the BHS results, a constant permeability offset is added ($k_{pores} \approx 4x10^{-18}$ m^2) to the model data, so as to permit the direct evaluation of the Guéguen and Dienes model permeability from the measured data. This method also provides an estimate of the permeability that is influenced by microcrack closure (i.e. the model crack permeability) rather than permeability due to near-equant porosity that is largely unaffected by effective pressure changes (i.e. the bulk permeability offset). A good fit to the experimental data is obtained with crack apertures of 0.8 μm sub-normal and 1.4 μm sub-parallel to the cross-bedding. Using equations (1) and (2), we calculate capillary radii of 0.06 μm to 0.29 μm sub-normal to cross-bedding and 0.04 μm to 0.18 μm sub-parallel to cross-bedding. This is less than the crack apertures as calculated from the Guéguen and Dienes model, but compares well with the average pore diameter calculated from mercury porosimetry (0.34 μm) (Figure 2), illustrating that COS contains a high proportion of crack-like porosity that dominated fluid flow and connectivity (in contrast to BHS).

Finally, TDG also exhibits considerable permeability anisotropy (Figure 8A), with permeability measured parallel to the microcrack fabric some three times higher than that normal to the microcrack plane. The application of the Kozeny-Carman approach to the dataset yields tortuosities within the TI plane of 0.0034 (X direction) and 0.0017 (Z direction) and a tortuosity normal to this plane (Y direction) of 1.0854. The average critical porosity is calculated as 0.71%. Thus, these data show similar trends to those seen for COS, but with a higher relative change in tortuosity parallel and normal to the TI plane. When modeling these permeability data via the Guéguen and Dienes model (Figure 8B), no

bulk offset is needed as the void space in this rock is composed purely of microcracks. The best model fit to the experimental data is obtained with an upper bound crack aperture of approximately 0.85 μm and a lower bound of approximately 0.45 μm. Thus, the permeability evolution sub-normal to the microcrack plane is modeled using a much lower crack aperture than for fluid flow sub-parallel to the microcrack plane. This is an artefact of our modeling, as we would expect the lower permeability normal to the crack plane to be due to the lower crack density in that orientation rather than a lower crack aperture. This may be expected intuitively if the permeability is treated in the form of microcrack density tensor, averaged over the plane of investigation. Alternatively, this could be taken into account in a more formal way, using the anisotropic formulation of the permeability equation (3) in the form of microcrack density tensor, rather than a scalar averaged value (Simpson et al., 2001).

6. Discussion

At one end of the spectrum of void space geometries studied, BHS is a well-sorted sandstone with predominantly near-equant porosity. Thus, any cracks are likely to be in the form of intergranular microcracks. The rock exhibits a P-wave velocity anisotropy of approximately 8% (Figure 3 and Benson et al., 2005). At the other end of the spectrum, TDG is a crystalline, microcracked granodiorite from a very young pluton (1.2 Ma) in the Japanese age (Kano and Tsuchiya, 2002). It has been suggested that both large scale joints and these microcracks were formed parallel to the cooling surface during cooling of the pluton (Kano and Tsuchiya, 2001). The result is an aligned crack fabric and a P-wave velocity anisotropy of approximately 10% (Figure 5) that is essentially co-incident at both the laboratory scale and the outcrop scale (Kano and Tsuchiya, 2002; Benson, 2004). The TI plane of these larger scale joints occurs at N4W/46W in the geographic reference frame, giving a Vp minimum (pole) in the direction of 94/44 (trend/plunge). Finally, COS is a mature sandstone, containing microstructural

features intermediate between the BHS and TDG end members, i.e. a mixture of near-equant pores and microcracks. This combination of different void space types is reflected in a room-pressure P-wave velocity anisotropy of 20% (Benson et al., 2003)

In all cases, results from the Kachanov (1994) model suggest a predominantly transversely isotropic fabric consistent with SEM, elastic wave velocity, and optical observations (Benson, 2004). Although all the rock types investigated here contain both cracks and pores, the rationale behind modeling permeability via a transversely isotropic crack model is to study the effect of microcrack-induced permeability variations where such cracks are solely responsible for transport property changes. We consider this to be a good approximation, given that many studies show how hydrostatic confinement is a key factor in microcrack closure (e.g. Dullien, 1979; Mavko et al., 1998), with a concomitant effect on fluid permeability.

The classic approach of Kozeny-Carman has been applied to all three rocks. When modelling the permeability-porosity variation (in this case, with effective pressure), the Kozeny-Carman method uses the concept of tortuosity. In this study, this is modified (Mavko and Nur, 1997) to take account of the non-zero 'threshold' porosity below which no flow is possible. For BHS, the Kozeny-Carman model requires a tortuosity of 4.1-4.5 in order fit the measured data. This is reasonable, given the high porosity (23%) and the SEM observations of its open and near-equant pore structure. For COS the Kozeny-Carman model also works well. Since the internal void fabric comprises a mixture of cracks and pores with an abundant cement, it is not unreasonable that the pore fabric resembles the tube-like structure modeled by Kozeny-Carman. COS exhibits a high degree of permeability anisotropy, giving rise to a higher tortuosity for fluid flow normal to the cross-bedding than for flow parallel to the cross-bedding. For TDG, a similar overall pattern as that for COS emerges, suggesting that although these two rocks are substantially different, fluid flow is controlled via the same fundamental processes. In

general, permeability values are lower for TDG, as might be expected for a crystalline rock of low porosity. In addition, TDG also exhibits a much lower tortuosity within its TI plane than the equivalent TI plane tortuosity in the case of COS. Taken together, these data suggest that tortuosity is linked to crack/pore connectivity whilst critical porosity reflects percolation. However, it should be noted that these fits are specific to both the rock type and also to the particular sample measured, i.e. this is a heuristic approach.

We have also applied the permeability model of Guéguen and Dienes (1989). This makes use of the crack density data as a function of effective pressure, as derived from the transverse isotropy implementation of the Kachanov (1994) model (Schubnel and Guéguen, 2003; Benson et al., 2006). This combined approach allows fluid permeability to be calculated as a function of crack density, for any desired crack aperture / aspect ratio. To allow the different rock types to be compared easily, the initial crack aspect ratio is set using the Morlier (1971) method which calculates an aspect ratio distribution function (Zimmerman, 1991). For the rocks studied here the aspect ratio ranges from 0.00042 for TDG to 0.0012 for BHS. As hydrostatic pressure is increased it is likely that crack closure is a key contributor to the decreasing permeability, primarily as a result of aperture reduction. In addition, however, increasing crack aspect ratio also plays a role, as thin cracks become progressively more ‘pinched out’. This may result in, for example, a number of cracks with a relatively high aspect ratio where a single crack of low aspect ratio was previously located, as opposing crack sides come into contact with each other due to surface roughness (Ayling et al., 1995).

Alternatively, equation (3) may be used to directly calculate crack aspect ratio via the measured permeability and the calculated crack density at each pressure step. In performing this calculation, however, we also apply the logic that crack aperture may only decrease with increasing pressure. This results in the necessity of increasing the aspect ratio with increasing effective pressure (which starts out

at its initial value, as calculated via the Morlier (1971) method). Thus we are able to recover the increase in crack aspect ratio with pressure via this iterative process (Figure 9A, Figure 10A, and Tables 2, 4 and 6). Whilst only an approximate method, this represents a good first order approximation in evaluating the changing crack parameters with effective pressure. A threshold of approximately 50 MPa is often cited (e.g. Mavko et al., 1998) as the pressure at which the majority of thin cracks are closed or pinched. This is consistent with our findings, which show a rapidly increasing aperture above this pressure (Figure 4, Figure 5). The forward solution (permeability) to the aperture and aspect ratio for COS and TDG, deduced via this method, is shown in Figure 9B (COS) and Figure 10B (TDG) which produces an excellent fit to the measured permeability data. This process was not performed for BHS, as no obvious permeability anisotropy or change with pressure is measured (figure 6A).

For BHS, our results show that crack permeability constitutes only 8% of the total permeability, but it this small proportion that is responsible for the change in permeability with increasing effective pressure. This is demonstrated via the Guéguen and Dienes approach, which shows that the small decrease in permeability is modeled well for crack apertures of approximately 5 μm to 30 μm, consistent with mercury porosimetry data (Figure 2). By contrast, for TDG all of the permeability is crack permeability. Finally, COS provides an intermediate case, with crack permeability providing 95% of the total permeability at 5 MPa but only 3 to 4% of the total permeability at 90 MPa. This demonstrates clearly how crack closure dominates the permeability decreases observed with increasing effective pressure.

However, it should be stressed once again that using isotropic models to fit data measured on anisotropic rock samples requires an element of caution. To mitigate any inaccuracies, we have therefore (1) calculated the crack density via the TI regression of elastic wave velocities, (2) calculated

and applied initial aspect ratios from data in known (orthogonal) directions to the Kozeny-Carman equation, and (3) used pAMS data as a guide in order to prepare samples along principal anisotropy axes. Previous work, investigating the accuracy of pore network models as compared to more simple permeability modeling strategies, has found that, if the microstructural data in a known direction is used, then isotropic models can produce data just as accurate as considerably more complicated strategies (e.g. Lock et al., 2004).

7. Conclusions

This study has explored the interplay between rock microstructure and permeability evolution for three rocks with contrasting microstructures at effective hydrostatic pressures up to 90 MPa. In order to measure the required parameters, an experimental apparatus was employed which is capable of measuring contemporaneous P-wave velocity, S-wave velocity, porosity and permeability under such conditions. The Kozeny-Carman and Guéguen and Dienes (1989) permeability relations, together with aspect ratio and crack density data from the Morlier (1971) and Kachanov (1994) methods, were used to investigate the contribution that microcrack closure has on permeability evolution in terms of crack aperture and aspect ratio. We successfully demonstrate that the change of permeability with pressure can be qualitatively related to the damage level of microcracked rock (crack aperture / aspect ratio) and that this general dependency holds even for rocks of high porosity and high bulk permeability.

The concept of tortuosity, as introduced via the Kozeny-Carman relation in equation (1), can be linked to a percolation threshold through the approximate relation $f \approx 1/\tau^2$. Despite calculation via a relatively simple model, both tortuosity and percolation produce useful insights when applied to the known anisotropic fabric of Crab Orchard sandstone and TDG. When applied along the principal permeability axes of Crab Orchard sandstone, a relatively high tortuosity is calculated for fluid flow

sub-normal to cross-bedding, with a low tortuosity obtained sub-parallel to cross-bedding. The goodness of fit further suggests that COS may have an internal pore structure which is well modeled by a network of capillaries, perhaps due to the diagenetic processes to which it has been subjected. For TDG, a similar pattern is seen, with high tortuosity calculated for flow normal to the TI plane. The relative change in tortuosity with increasing effective pressure, both parallel and normal to the TI plane (x 500), is much greater than for COS (x 2); this is consistent with its crystalline, microcracked fabric. For Bentheim sandstone, however, the Kozeny-Carman approach does not produce meaningful results, due to the open and near-equant pore fabric in this rock. Using the model of Guéguen and Dienes (1989), however, we show that, even for this highly permeable rock, the permeability change with increasing effective pressure may be predicted from microcrack permeability alone. We further show that, up to approximately 40 MPa, the permeability of all rocks tested in this study may be represented via a single crack aperture; within the limits of anisotropy.

In general, studies of the physical properties of rocks often focus on the measurement of a single parameter, and its changes. In this study, this has been expanded to an experimental investigation of permeability evolution at elevated pressures with simultaneous measurement of changes in complementary physical properties that allows the application of permeability models to the problem. We are thus able to conclude that microcracks are the dominant feature influencing permeability decrease with increasing effective pressure; that crack aperture variations may be used to explain such permeability changes; and that a constant, background permeability level is inherent in all of these rocks. We also conclude that, whilst the procedure of applying microstructural parameters taken in known orthogonal directions can indeed be used in isotropic models and applied to anisotropic rocks, this is probably at the limit of such strategies. For the rocks tested in this study, permeability anisotropy is dominated by void space anisotropy, whether this is as a result of a well sorted grain matrix; a mature cemented and altered matrix; or a predominantly micro-fractured matrix.

8. Acknowledgements

This work was supported by the UK Natural Environment Research Council (NERC) through award NER/S/A/2001/06507 to PB. PB and PM would like to thank Catherine Stafford and Toru Takahashi (Fracture Research Institute, Tohoku University, Japan) for supplying the Takidani granite, and the Silvara Stone Company (Crossville, TN, USA) for supplying the Crab Orchard Sandstone. AS kindly thanks Paul Young for financial assistance in the form of a Canada Natural Sciences and Engineering Research Council (NSERC) supported postdoctoral fellowship. The authors thank Yves Guéguen, Ernie Rutter, and an anonymous reviewer for helpful comments that greatly improved the manuscript.

9. References

Ayling, M.R., P.G. Meredith, and S.A.F. Murrell (1995), Microcracking during triaxial deformation of porous rocks monitored by changes in rock physical properties. 1. elastic-wave propagation measurements on dry rocks. *Tectonophysics*, 245, 205-221.

Benson, P.M., P.G. Meredith and E.S. Platzman (2003), Relating pore fabric geometry to elastic and permeability geometry in Crab Orchard Sandstone: A Laboratory study using magnetic ferrofluid. *Geophys. Res. Lett.*, 30(19), 1976, doi:10.1029/2003GL017929

Benson, P. M. (2004), Experimental study of void space, permeability and elastic anisotropy in crustal rock under ambient and hydrostatic pressure, Ph.D. thesis, 272pp., University of London, London.

Benson, P. M., P. G. Meredith, E. S. Platzman, and R. E. White (2005), Pore fabric shape anisotropy in porous sandstone and its relation to elastic and permeability anisotropy under isostatic pressure, *Int. Journal. Rock. Mech.*, 42, 890-899, doi:10.1016/j.ijrmms.2005.05.003.

Benson, P.M, A. Schubnel, S. Vinciguerra, C. Trovato, P. Meredith, and R. P. Young (2006), Modeling the permeability evolution of microcracked rocks from elastic wave velocity inversion at elevated isostatic pressure, *J. Geophys. Res.*, 111, B04202, doi:10.1029/2005JB003710.

Berge, P. A., G.J. Fryer and R.H. Wilkens (1992), Velocity-Porosity Relationships in the upper Oceanic Crust: Theoretical Considerations. *J. Geophys. Res.*, 97, 15239-15254.

Bernabe, Y., U. Mok, and B. Evans (2003), Permeability-porosity relationships in rocks subjected to various evolution processes. *Pure and applied Geophysics*, 160, 937-960

Bourbie, T., and B. Zinszner (1985), Hydraulic and elastic properties as a function of porosity in Fontainebleau Sandstone. *J. Geophys. Res*., 90, 11524-11532.

Brace, W. F., J. B. Walsh, and W. T. Frangos (1968), Permeability of Granite under high pressure, *J. Geophys. Res., 73*, 2225-2236.

Brace, W. F. (1980), Permeability of crystalline and argillaceous rocks, *Int. J. Rock Mech. Min. Sci. Geomech. Abstr., 17*, 241-251.

Carman, P.C. (1961). *L'écoulement des Gas á Travers les Milieux Poreux, Bibliothéque des Sciences et Techniques Nucléaires*, 198pp. Presses Universitaires de France, Paris,

Dullien, F. (1979), *Porous media: Fluid transport and pore structure*. 396pp. Academic Press.

Guéguen, Y., and J. Dienes (1989), Transport Properties of Rocks from Statistics and Percolation, *Mathematical Geology*, *21*, 1-13.

Guéguen, Y., and A. Schubnel (2003), Elastic wave velocities and permeability in cracked rocks, *Tectonophysics*, 370, 163-176.

Guéguen, Y., and V. Palciauskas (1994), *Introduction to the Physics of Rocks*. 292pp. Princeton University press. New Jersey.

Jones, C., and P. Meredith (1998), An experimental study of elastic wave propagation anisotropy and permeability anisotropy in an illitic shale. Presented at Eurock 98, Proc. SPE/ISRM Rock Mechanics in Petroleum Engineering, vol.1, 307-314, Trondheim, Norway.

Kano, S., and N. Tsuchiya (2002), Parallelepiped cooling joint and anisotropy of P-wave velocity in the Takidani granitoid, Japan Alps. *J. Volcanology and Geothermal Res.*, *114*, 465-477.

Kachanov, M. (1980), Continuum model of medium with cracks. *J. Eng. Mech. Div.*, 106, 1039-1051

Kachanov, M. (1994), Elastic solids with many cracks and related problems, *Adv. Appl. Mech.*, *30*, 259-445.

Klein, E., P. Baud, T. Reuschlé, and T-f. Wong (2001), Mechanical behaviour and Failure mode of Bentheim sandstone under triaxial compression. *Phys. Chem. Earth(A).*, 26, 21-25.

Klimentos, T. (1991), The effects of porosity-permeability-clay content on the velocity of compressional waves. *Geophysics*, 56, 1930-1939.

Lo, Tien-when, Karl B. Coyner, and M. Nafi Toksoz (1986), Experimental determination of elastic anisotropy of Berea sandstone, Chicopee shale, and Chelmsford granite. *Geophysics*, 51, 164-171.

Lock, P.A., Jing, X.D., and R.W. Zimmerman (2004), Comparison of methods for upscaling permeability from the pore scale to the core scale. *J. Hydraul. Res.*, 42, 3-8.

Mavko, G., T. Mukerji, and J. Dvorkin (1998), *The rock physics handbook: tools for seismic analysis in porous media*. 329pp., Cambridge University Press, Cambridge.

Mavko, G., and A. Nur (1997), The effect of a percolation threshold in the Kozeny-Carman relation. *Geophysics*, 62, 1480-1482.

Morlier, P. (1971), Description of the state of rock fracturization through simple non-destructive tests. *Rock mechanics*, 3, 125-138.

Rasolofosaon, P.N.J. and B.E. Zinszner (2002), Comparison between permeability anisotropy and elastic anisotropy of reservoir rocks. *Geophysics*, 67, 230-240.

Sayers, C. M. and M. Kachanov (1995), Microcrack induced elastic wave anisotropy of brittle rocks, *J. Geophys. Res.*, *100*, 4149-4156.

Scheidegger, A.E. (1974), *The Physics of Flow Through Porous Media*, 3rd Ed., 353 pp., Univ. Toronto Press, Toronto.

Schubnel, A. and Y. Guéguen (2003), Dispersion and Anisotropy in Cracked Rocks, *J. Geophys. Res.*, *108*, 2101, doi:10.1029/2002JB001824.

Simpson, G., Y. Guéguen, and F. Schneider (2001), Permeability enhancement due to microcrack dilatancy in the damage regime, *J. Geophys. Res.*, *106*, 3999-4016.

Stearns, R.G., 1954, The Cumberland Plateau Overthrust and Geology of the Crab Orchard Mountains area, Tennessee. Tennessee Division of Geology Bulletin 60, pp47

Walsh, J.B., and W.F. Brace (1984), The effect of pressure on porosity and the transport properties of rock. *J. Geophys. Res.*, 89(B11), 9425-9431.

Wendt, A.S., I.O. Bayuk, S.J. Covey-Crump, R. Wirth, and G.E. Lloyd (2003), An experimental and numerical study of the microstructural parameters contributing to the seismic anisotropy of rocks. *J. Geophys. Res.*, 108(B8), 2365, doi:10.1029/2002JB001915

Wyllie, M.R.J., A.R. Gregory, and L.W. Gardner (1958), An experimental investigation of factors affecting elastic wave velocities in porous media. *Geophysics*, 23, 459-493.

Zimmerman, R.W. (1991), *Compressibility of Sandstones*, 173 pp., Elsevier, New York.

Figure Captions

Figure 1. Top: SEM pictures of freshly broken surfaces of each rock type. From left to right, Bentheim sandstone, Crab Orchard sandstone and Takidani granite. Bottom: principal void space directions determined via the use of pore space anisotropy of magnetic susceptibility (pAMS), for (A): Bentheim sandstone, (B): Crab Orchard sandstone, and (C): Takidani granite. Open circles denote pore anisotropy minima, open squares denote anisotropy maximum values, with open triangles denoting the statistically-derived 'intermediate' orientation of the average void space ellipsoid. Solid symbols denote each mean of these data, with 95% confidence ellipses (after Benson, 2004).

Figure 2. Left: Mercury porosimetry data for BHS, COS and TDG, yielding average pipe radii of approximately 15.6μm, 0.17μm and 0.04μm respectively. Right: The experimentally derived porosity – effective pressure (Peff=Pc-Pp) evolution for each rock type.

Figure 3. Left: The measured Vp increase with effective pressure for Bentheim sandstone. To test for permeability anisotropy, measurements were made in three orthogonal directions (X, Y, and Z) with respect to the same common co-ordinate system illustrated in figure 1. Right: Using the Vp and Vs data (not shown, see table 1) with increasing Peff, initial aspect ratio 'ζ' was calculated via the method of Morlier (1971). Crack density was then computed using this data (Vp, Vs, ζ) input to the model of Kachanov (1994). See text for detail.

Figure 4. Left: The measured Vp increase with effective pressure for Crab Orchard sandstone. To test for permeability anisotropy, measurements were made in three orthogonal directions (X, Y, and Z) with respect to the same common co-ordinate system illustrated in figure 1. Right: Using the Vp and Vs data (not shown, see table 2) with increasing Peff, initial aspect ratio 'α' was calculated via the method

of Morlier (1971). Crack density was then computed using this data (Vp, Vs, α) input to the model of Kachanov (1994). See text for detail.

Figure 5. Left: The measured Vp increase with effective pressure for Takidani granite. To test for permeability anisotropy, measurements were made in three orthogonal directions (X, Y, and Z) with respect to the same common co-ordinate system illustrated in figure 1. Right: Using the Vp and Vs data (not shown, see table 2) with increasing Peff, initial aspect ratio 'α' was calculated via the method of Morlier (1971). Crack density was then computed using this data (Vp, Vs, α) input to the model of Kachanov (1994). See text for details.

Figure 6. Left: Experimentally measured permeability evolution with increasing effective pressure for Bentheim sandstone. Lines denote the tortuosity fit calculated via the Kozeny-Carman relation. Right: The same experimental permeability data; this time compared to a theoretical evolution of permeability due to cracks only, calculated via the Guéguen and Dienes (1989) model. Guéguen and Dienes model values are normalized to the 'pores only' measurement (8.1×10^{-13}), to illustrate the effect of changing crack aperture size upon the permeability decrease with pressure.

Figure 7. Left: Crab Orchard sandstone experimental permeability (symbols) and Kozeny-Carman least-square fit (lines) as a function of effective pressure. In this case, 'X' and 'Y' directional permeability (XY plane) is coincident to the visible crossbedding. Permeability sub-normal to crossbedding is approximately half of that sub-parallel to crossbedding. Tortuosities of 0.013 and 0.028 were derived for fluid flow parallel and normal to bedding respectively. Right: Comparison between experimental permeability (symbols) and theoretical Guéguen and Dienes crack permeability (dashed lines) with increasing effective pressure for Crab orchard sandstone. The calculated Guéguen and

Dienes values are again normalized to the 'pores only' permeability value of 4 $x10^{-18}$ to highlight the comparison between experimental bulk permeability decrease, and theoretical permeability decrease due to microcracks.

Figure 8. Caption (revised): Left: Takidani granite experimental permeability (symbols) and Kozeny-Carman least-square fit (lines) as a function of effective pressure. Permeability sub-parallel to the microcrack orientation is approximately three times that sub-normal to crack orientation. Tortuosities of 0.0034, 0.0017 and 1.0854 were derived for fluid flow in the X, Z and Y directions respectively. Right: Comparison between experimental permeability (symbols) and theoretical Guéguen and Dienes crack permeability (dashed lines) with increasing effective pressure for Takidani granite. As this rock type is purely cracked, no normalization process is required to compare the variation of theoretical permeability to experimental permeability.

Figure 9. Left: The calculated aperture for COS as a function of effective pressure. The working assumption that the aperture may only decrease was used with the computed (fixed) crack density evolution. To avoid breaking this assumption, aspect ratio increases with increasing pressure, as presented earlier in figure 4. Right: the forward model (permeability) due to the changing crack parameters, compared to experimental data (symbols).

Figure 10. Left: The calculated aperture for TDG as a function of effective pressure. The working assumption that the aperture may only decrease was used with the computed (fixed) crack density evolution. To avoid breaking this assumption, aspect ratio increases with increasing pressure, as presented earlier in figure 5. Right: the forward model (permeability) due to the changing crack parameters, compared to experimental data (symbols).

Tables

Table 1. BHS Laboratory data

Measurement axis	Pc-Pp, MPa	K, m^2	Vp, m/s	Vs, m/s	Porosity, fractional
	5.63	8.65E-13	3983.67	2253.91	0.2215
	10.15	8.54E-13	4037.89	2278.16	0.2205
	14.98	8.75E-13	4100.75	2305.53	0.2197
	20.36	8.63E-13	4153.53	2328.22	0.2192
	29.55	8.26E-13	4187.63	2353.92	0.2183
X	39.91	8.35E-13	4216.77	2369.14	0.2173
	49.85	8.52E-13	4248.44	2379.52	0.2167
	60.15	8.32E-13	4262.21	2388.59	0.2160
	69.85	8.38E-13	4281.09	2396.23	0.2154
	79.67	8.60E-13	4289.14	2401.99	0.2147
	90.23	8.48E-13	4299.61	2405.95	0.2142
	5.25	8.33E-13	3877.35	2162.40	0.2296
	10.53	8.05E-13	3963.81	2241.00	0.2283
	15.37	8.32E-13	4004.53	2258.69	0.2277
	20.11	8.67E-13	4033.75	2272.36	0.2271
	29.91	8.16E-13	4058.17	2287.08	0.2261
Y	39.93	8.09E-13	4086.23	2295.11	0.2253
	49.94	8.08E-13	4097.50	2300.54	0.2247
	59.99	8.03E-13	4109.05	2306.68	0.2241
	69.79	8.06E-13	4130.39	2314.02	0.2234
	79.60	7.91E-13	4131.59	2318.77	0.2228
	89.81	8.14E-13	4143.98	2322.48	0.2220
	5.10	7.52E-13	3719.80	2124.89	0.2181
	10.34	7.96E-13	3858.35	2163.77	0.2169
	15.41	8.03E-13	3906.37	2194.83	0.2161
	20.34	8.09E-13	3950.25	2210.99	0.2154
	29.84	8.46E-13	3981.02	2230.51	0.2144
Z	39.51	8.33E-13	4008.40	2248.60	0.2137
	50.03	8.13E-13	4037.88	2266.31	0.2128
	59.81	8.13E-13	4053.06	2274.15	0.2122
	69.97	8.37E-13	4061.63	2280.53	0.2115
	80.01	7.82E-13	4067.83	2285.11	0.2108
	90.02	8.07E-13	4077.23	2289.22	0.2101

Table 2. BHS model parameters (E_0=32.7 GPa, υ_0=0.271)

Pc-Pp, MPa	Crack density (no unit)	Aspect ratio (no unit)
5.33	0.37	0.0012
10.34	0.27	0.0012
15.25	0.23	0.0012
20.27	0.2	0.0012
29.77	0.17	0.0012
39.78	0.15	0.0012
49.94	0.13	0.0012
59.98	0.12	0.0012
69.87	0.1	0.0012
79.76	0.1	0.0012
90.02	0.09	0.0012

Table 3. COS Laboratory data

Measurement axis	Pc-Pp, MPa	K, m^2	Vp, m/s	Vs, m/s	Porosity, fractional
	5.19	1.27E-16	4489.26	2540.74	0.0480
	10.17	8.63E-17	4567.68	2642.54	0.0473
	16.06	5.72E-17	4664.80	2672.65	0.0467
	20.65	4.18E-17	4750.89	2704.93	0.0464
	29.30	2.97E-17	4841.13	2727.31	0.0458
X	39.56	2.32E-17	4902.48	2768.13	0.0455
	49.77	1.65E-17	4976.20	2820.41	0.0452
	59.31	1.25E-17	5018.51	2861.46	0.0450
	69.78	9.89E-18	5060.83	2900.53	0.0447
	79.21	6.26E-18	5090.30	2934.99	0.0445
	90.53	4.30E-18	5136.25	2965.62	0.0444
	5.19	1.00E-16	4489.17	2526.47	0.0506
	10.12	6.82E-17	4578.03	2594.80	0.0498
	15.09	4.51E-17	4665.80	2627.88	0.0492
	20.08	3.60E-17	4720.97	2659.34	0.0487
	29.42	2.63E-17	4842.03	2695.54	0.0481
Y	39.30	1.87E-17	4921.21	2772.32	0.0477
	49.58	1.11E-17	4979.99	2828.83	0.0473
	59.76	8.54E-18	5041.06	2873.48	0.0471
	69.97	6.91E-18	5088.20	2926.16	0.0469
	79.57	4.88E-18	5126.31	2943.80	0.0467
	90.10	3.24E-18	5150.39	2967.14	0.0466
	4.63	4.95E-17	4337.27	2489.71	0.0470
	10.20	3.48E-17	4451.85	2539.60	0.0462
	14.81	2.41E-17	4541.23	2584.04	0.0457
	20.43	1.73E-17	4621.27	2626.48	0.0454
	30.02	1.24E-17	4715.60	2671.54	0.0448
Z	40.46	7.32E-18	4828.07	2751.10	0.0444
	50.14	5.91E-18	4871.62	2809.89	0.0442
	60.25	4.08E-18	4947.87	2852.04	0.0440
	70.29	3.83E-18	4974.54	2892.33	0.0438
	80.08	2.72E-18	5029.58	2934.20	0.0436
	89.64	2.63E-18	5061.67	2962.19	0.0435

Table 4. COS model parameters (E_0=55.28 GPa, υ_0=0.197)

Pc-Pp, MPa	Parallel			Normal		
	Crack density	Aspect ratio	Aperture, μm	Crack density	Aspect ratio	Aperture
4.9	0.43	0.00068	1.69	0.43	0.00058	1.19
10.2	0.33	0.00068	1.58	0.34	0.00058	1.11
14.9	0.27	0.00068	1.41	0.27	0.00058	1.02
20.3	0.21	0.00068	1.38	0.21	0.00058	0.96
29.7	0.15	0.00068	1.37	0.15	0.00058	0.94
39.9	0.09	0.00082	1.37	0.09	0.00058	0.86
49.9	0.06	0.00082	1.32	0.06	0.00063	0.85
60.0	0.05	0.00082	1.22	0.05	0.00063	0.66
70.1	0.03	0.00100	1.22	0.03	0.00091	0.66
79.8	0.02	0.00100	1.09	0.02	0.00091	0.45
89.9	0.01	0.00100	1.01	0.01	0.00148	0.45

Table 5. TDG Laboratory data

Measurement axis	Pc-Pp, MPa	K, m^2	Vp, m/s	Vs, m/s	Porosity, fractional
	4.58	2.11E-17	5783.03	3023.73	0.00926
	10.49	1.65E-17	5829.57	3042.37	0.00896
	14.76	1.49E-17	5879.33	3060.48	0.00876
	21.11	1.37E-17	5912.12	3077.03	0.00861
	29.56	9.97E-18	5940.75	3101.30	0.00840
X	40.33	7.87E-18	6005.65	3125.92	0.00826
	50.24	5.52E-18	6026.65	3150.59	0.00815
	60.88	5.23E-18	6052.43	3172.42	0.00798
	70.14	3.19E-18	6081.59	3189.42	0.00792
	80.63	5.03E-18	6102.12	3203.95	0.00777
	89.50	4.84E-18	6129.30	3207.50	0.00771
	5.07	1.12E-17	5693.76	2933.98	0.00898
	9.65	9.00E-18	5806.15	2955.47	0.00882
	15.08	6.86E-18	5858.21	2971.22	0.00868
	20.25	4.78E-18	5888.42	2980.47	0.00856
	30.19	3.80E-18	5908.71	3000.99	0.00844
Y	39.90	3.60E-18	5935.37	3019.35	0.00833
	50.04	1.51E-18	5961.65	3042.46	0.00818
	59.80	1.84E-18	5985.85	3064.53	0.00809
	69.89	1.76E-18	6045.14	3088.78	0.00805
	79.87	1.34E-18	6068.38	3106.59	0.00798
	90.03	1.54E-18	6085.57	3119.12	0.00794
	4.91	3.11E-17	5787.70	2963.11	0.00922
	9.70	2.27E-17	5844.06	2983.41	0.00900
	14.92	1.63E-17	5888.73	3001.15	0.00884
	20.03	1.10E-17	5936.95	3015.63	0.00876
	29.61	9.27E-18	5989.45	3037.41	0.00856
Z	39.84	7.50E-18	6024.61	3055.43	0.00842
	49.60	7.22E-18	6064.50	3069.12	0.00831
	59.74	3.90E-18	6117.30	3092.69	0.00822
	69.50	5.38E-18	6146.74	3103.93	0.00818
	79.85	4.02E-18	6171.19	3114.49	0.00811
	89.22	2.84E-18	6190.38	3121.13	0.00806

Table 6. TDG model parameters (E_0=81.88 GPa, υ_0=0.32)

Pc-Pp, MPa	Parallel			Normal		
	Crack density	Aspect ratio	Aperture, μm	Crack density	Aspect ratio	Aperture
4.75	0.47	0.00047	0.94	0.49	0.00042	0.64
10.10	0.43	0.00047	0.85	0.45	0.00042	0.60
14.84	0.39	0.00047	0.85	0.42	0.00042	0.54
20.57	0.38	0.00047	0.79	0.4	0.00042	0.47
29.58	0.35	0.00052	0.79	0.37	0.00046	0.47
40.09	0.33	0.00054	0.79	0.34	0.00062	0.47
49.92	0.31	0.00059	0.79	0.32	0.00062	0.35
60.31	0.28	0.00068	0.79	0.3	0.00099	0.35
69.82	0.26	0.00092	0.79	0.27	0.0016	0.35
80.24	0.25	0.0012	0.79	0.26	0.0016	0.34
89.36	0.23	0.00163	0.79	0.24	0.0028	0.34

Figures

Figure 1:

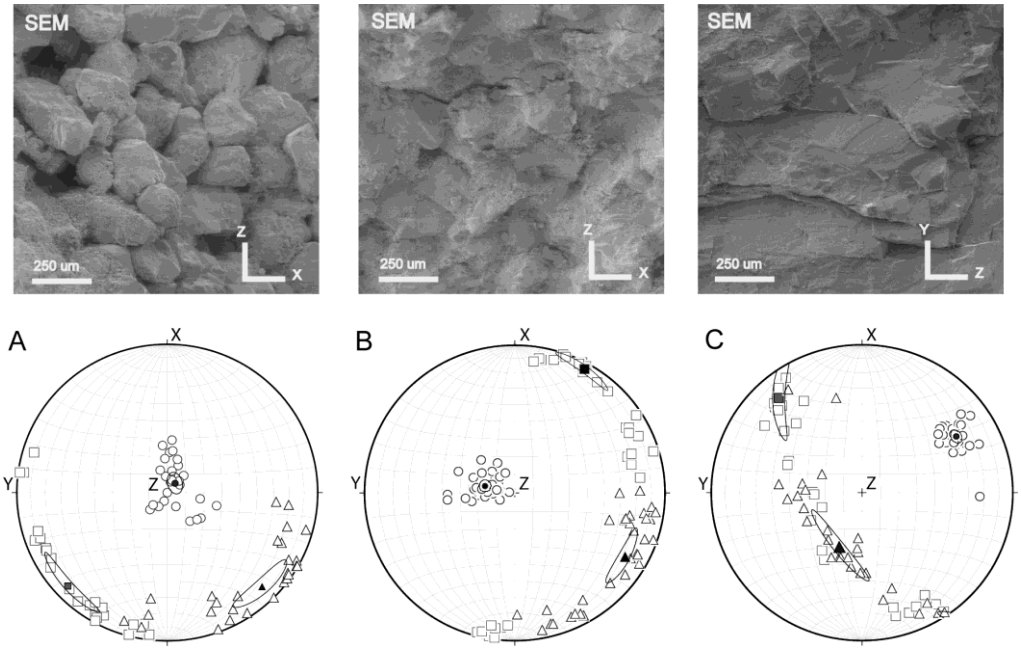

Figure 2:

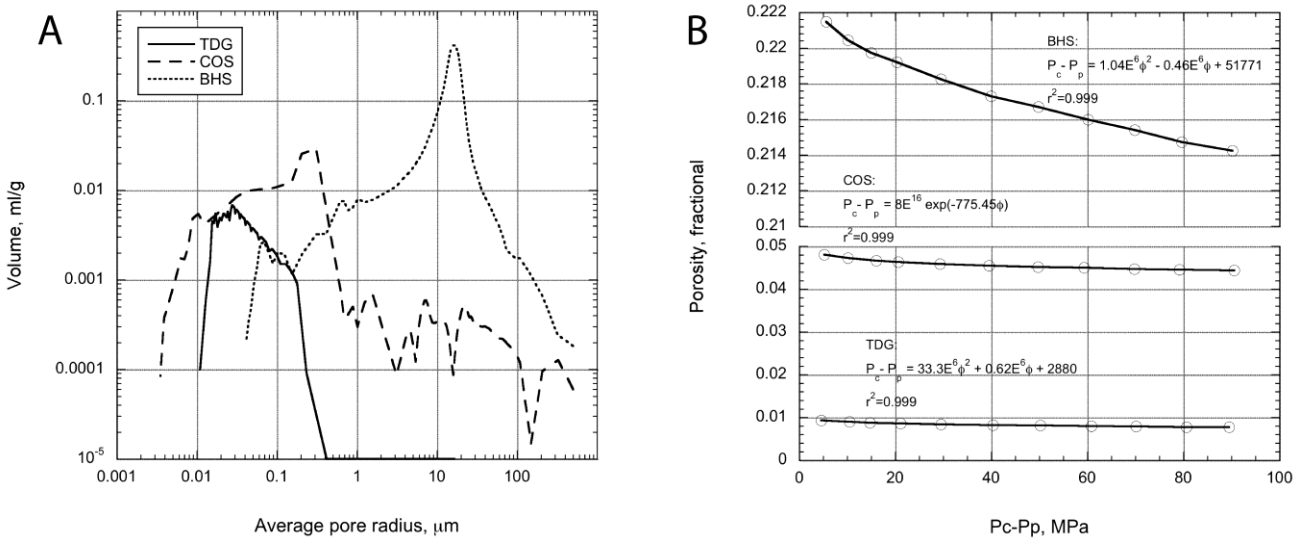

Figure 3:

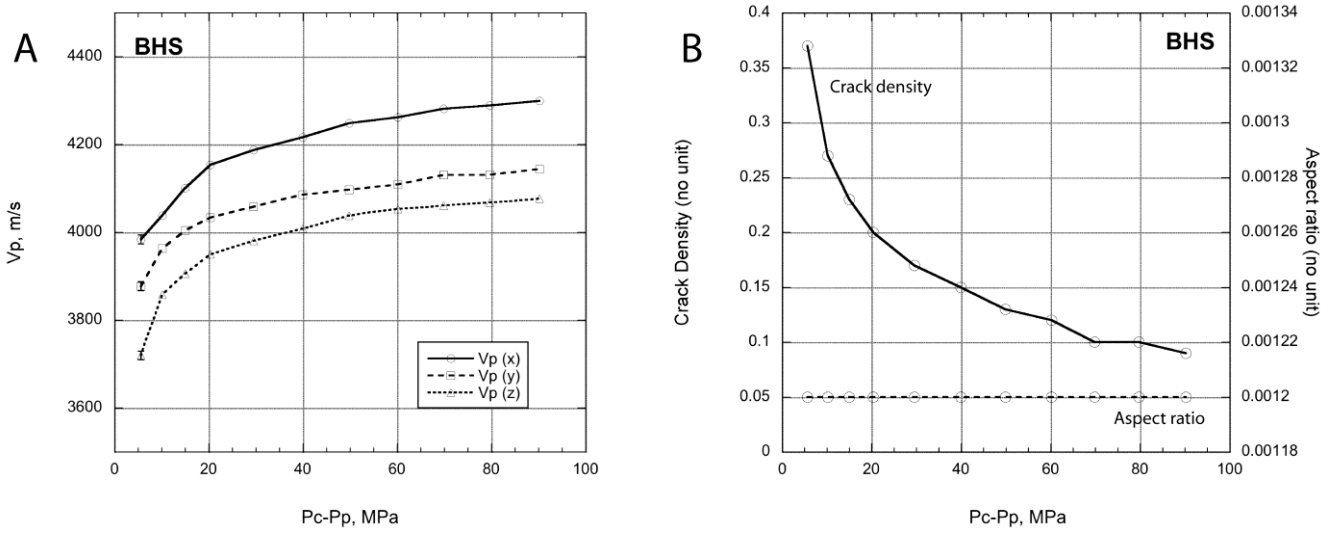

Figure 4:

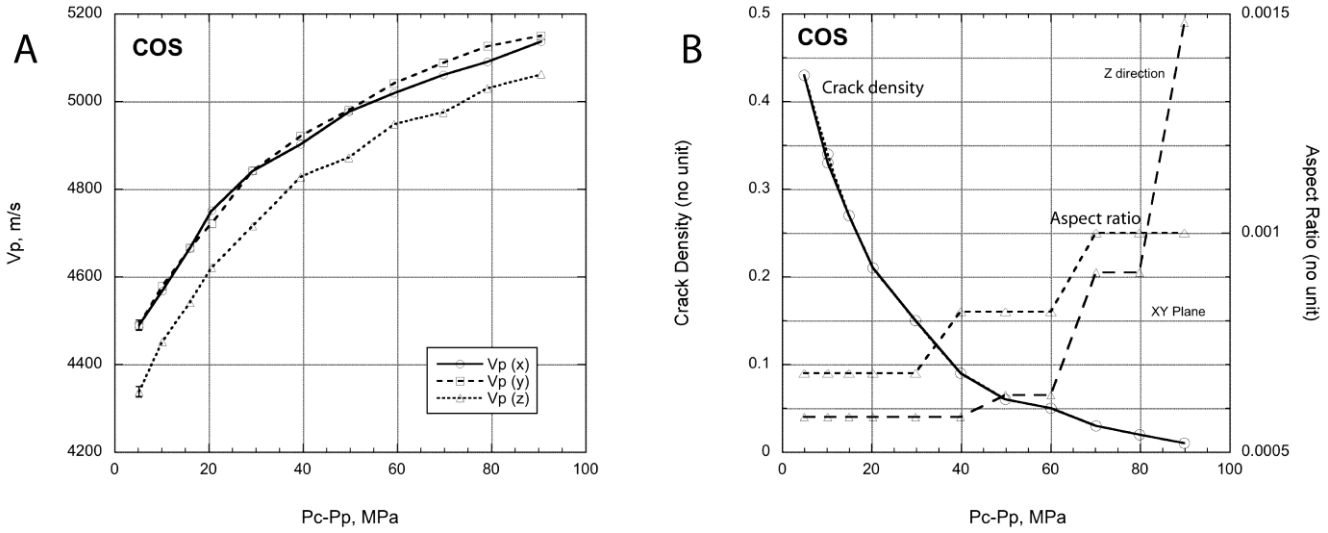

Figure 5:

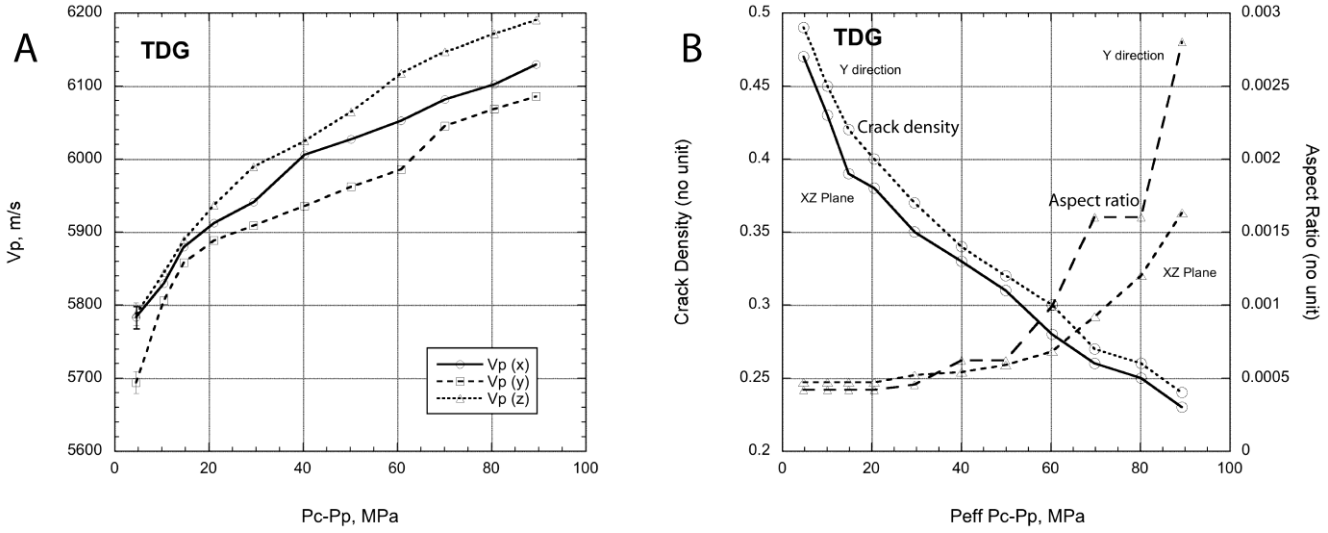

Figure 6:

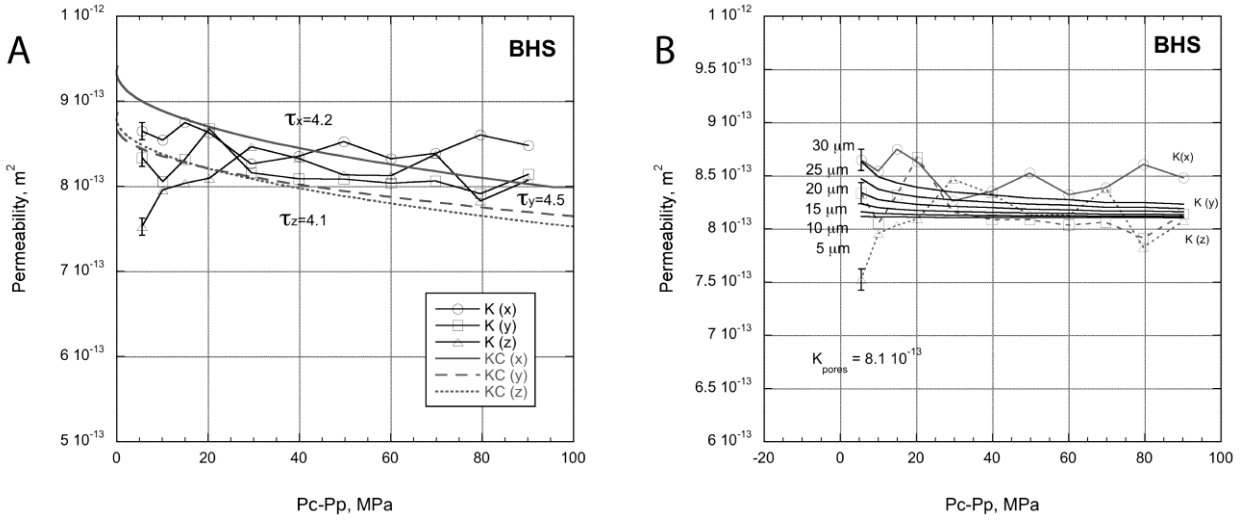

Figure 7:

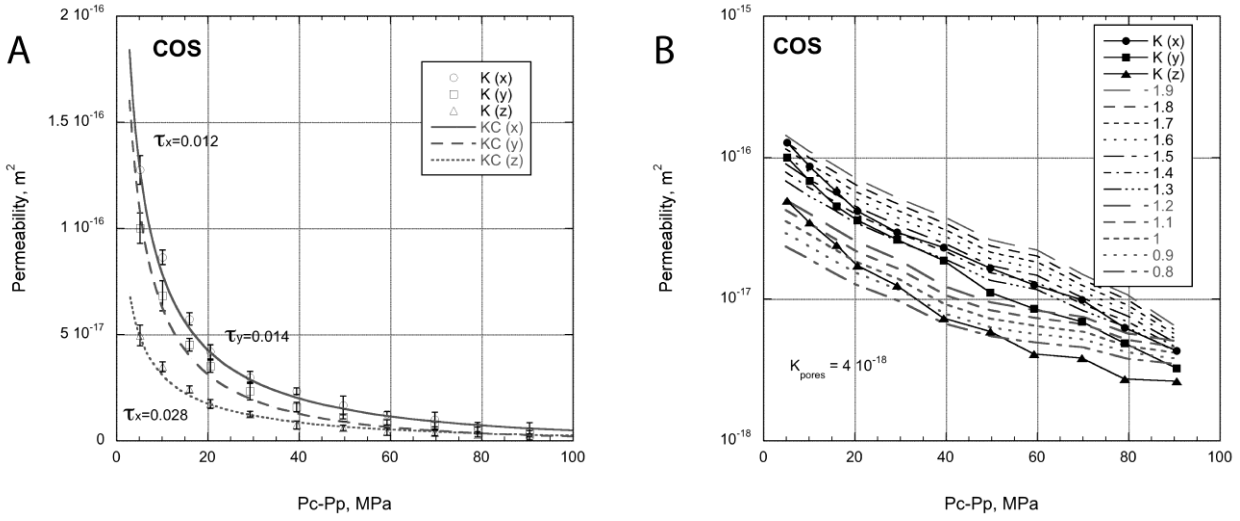

Figure 8:

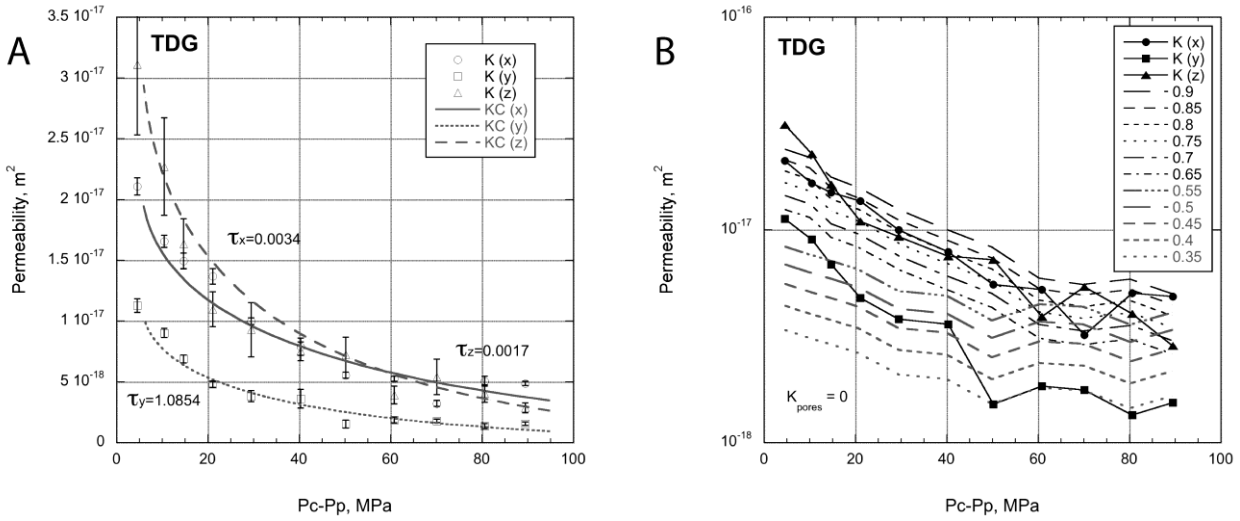

Figure 9:

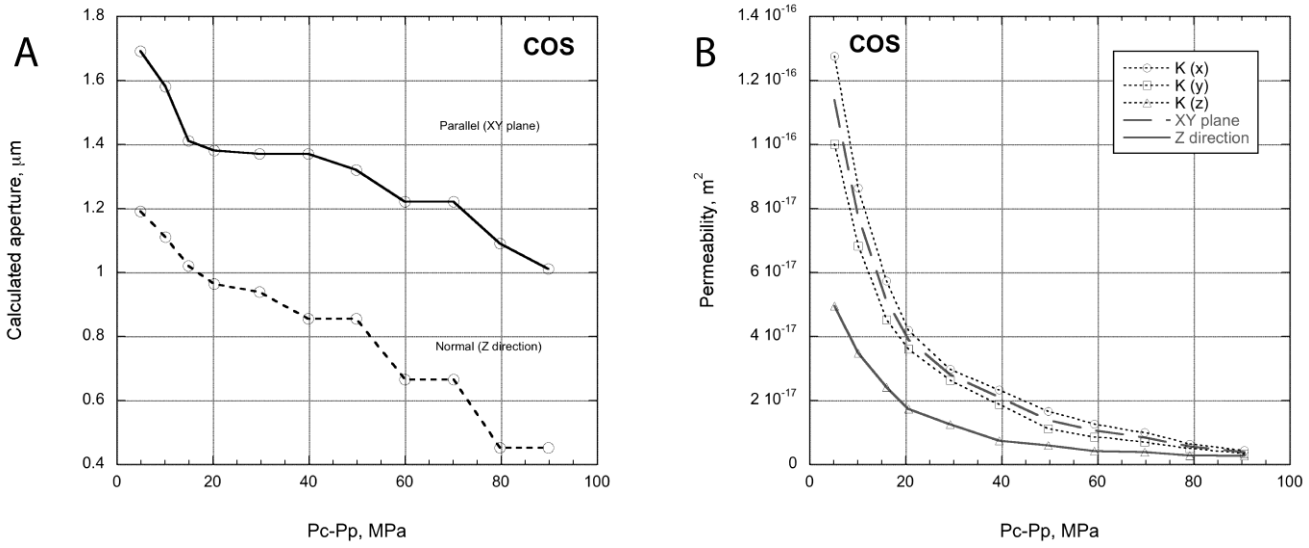

Figure 10: